High harmonic generations triggered by the intense laser field in GaAs/Al$_x$Ga$_{1-x}$As honeycomb quantum well wires

B.O. Alaydin [a,b], D. Altun [a,c], O. Ozturk [d], E. Ozturk [e,*]

[a] Nanophotonic Application and Research Center, Sivas Cumhuriyet University, 58140, Sivas, Turkiye
[b] Department of Electronics and Automation, Sivas Cumhuriyet University, 58140, Sivas, Turkiye
[c] Department of Electricity and Energy, Sivas Cumhuriyet University, 58140, Sivas, Turkiye
[d] Department of Nanotechnology Engineering, Sivas Cumhuriyet University, 58140, Sivas, Turkiye
[e] Department of Physics, Sivas Cumhuriyet University, 58140, Sivas, Turkiye

ARTICLE INFO

ABSTRACT

Under constant electric and magnetic fields, the potential profile of the honeycomb quantum well wire (HQWW) is studied for varying intense laser fields to trigger and optimize high harmonics (nonlinear optical rectification, second and third harmonic generation coefficients). The finite element method has been used to simulate wavefunctions and their corresponding energy levels under effective mass approximation. We have shown that an intense laser field reshapes the potential profile of the HQWW, and this results in maximum and minimum for dipole moment matrix elements and energy differences. The increase and decrease of energy differences create blue and red shifts in the optical spectrum. In the end, we have calculated nonlinear optical rectification as $11.1 \times 10{-}5$ m/V. The second harmonic generation coefficient is found as $18.4 \times 10{-}7$ m/V which is three times and a lot bigger than bulk GaAs and GaAs/AlGaAs superlattice. The third harmonic generation coefficient is calculated as $6.2 \times 10{-}15$ m2/V2. As a conclusion, we have shown that HQWW can be used in harmonic generation-based optical devices.

1. Introduction

Over the last three decades, semiconductor devices have shown extraordinarily high performances due to the deep understanding of their structures. The remarkable advancement in the experimentally grown low dimensional quantum well-based technologies results in low-cost and efficient devices [1–4]. Especially, in the field of photodiode and laser research, important progress has been made [5–7].

However, studies about two and three-dimensional systems are still in progress due to experimental difficulties about the production and complex physics behind them [8–12]. Particularly, complex second-order differential equations and computational problems have increased the difficulty of theoretical analysis [13–17]. This causes new perspectives to analyze multi-dimensional systems like reducing to one-dimension which does not support comprehensive knowledge.

Up to now, optical properties of two-dimensional systems have been considered for different structures [18,19]. Barseghyan et al. has focused on the absorption properties of the GaAs/Ga$_{1-x}$Al$_x$As cylindrical quantum well wire (QWW) [20]. The binding energy and photoionization cross-section of the impurity in QWW in electric and magnetic fields has been analyzed by Mughnetsyan et al. [21]. Optical rectification (OR) is studied for laterally coupled Al$_x$Ga$_{1-x}$As/GaAs QWW by Liu et al. [22]. The second and third harmonics are calculated for quantum ring by Duque et al. [23]. Nonlinear optical properties of QWW and quantum dot (QD) have been simulated for donor impurity states under external fields [24–26]. Terahertz laser field manipulation on the electronic and nonlinear optical properties of laterally coupled QWWs for a 40% Aluminum containing barrier has been investigated by Liu et al. also [27]. Anisotropic optical absorption in QWWs induced by high-frequency laser field has been deeply studied by Niculescu et al. [28]. They have shown variations of the total optical absorption coefficient and refraction coefficients under a strong laser field. The effect of the magnetic field on the linear and nonlinear optical properties of co-axial QWWs has been examined by Karimi et al. [29]. THz laser field effect on the optical properties of cylindrical QWWs has been shown by Burileanu and Radu [30]. Impurity-related optical properties of the QWW have been discussed by Montes et al. [31]. Binding energy and polarizability in GaAs QWW have been investigated by Duque et al.

* Corresponding author.
  E-mail address: eozturk@cumhuriyet.edu.tr (E. Ozturk).
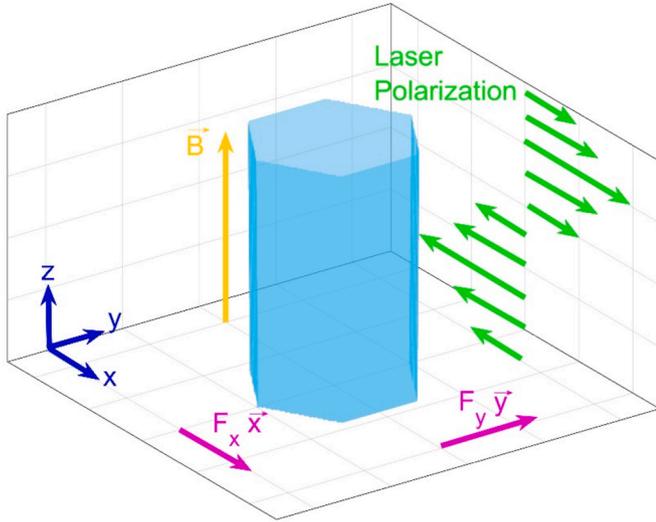
Fig. 1. Schematic cross-section of GaAs/Al$_x$Ga$_{1-x}$As HQWW and direction of external fields.

[32].

In this paper, we have focused on the high harmonic generations (HHGs) apart from the existing studies in the literature. We have studied nonlinear optical rectification (NOR), second harmonic generation (SHG), and third harmonic generation (THG) coefficients of the GaAs/Al$_x$Ga$_{1-x}$As honeycomb quantum well wire (HQWW) for the first time to our knowledge in the literature. A varying intense laser field (ILF) has been used to trigger high harmonics for the constantly applied electric field (EF) and magnetic field (MF). The paper contains three parts: i) In section II, we have given theoretical aspects of the HQWW, ii) In section III, we have discussed the computational results, iii) we have finished the paper with the conclusion in section IV.

2. Theory

The time-independent Hamiltonian of the two-dimensional GaAs/AlGaAs Hexagonal Quantum Well Wire (HQWW) heterojunction is given in Eq. (1),

$$H = \frac{1}{2m^*}\left(\vec{P} + e\,\vec{A}(\vec{r})\right)^2 + e\,\vec{F}(\vec{r}) \bullet \vec{r} + V(\vec{r}) \tag{1}$$

Development of Eq. (2) from Eq. (1) is well described in references [33,34]. The two-dimensional Schrödinger equation is a reduced form of three dimensional one [35,36]:

$$\left(-\frac{\hbar^2}{2m^*}\left(\frac{d^2}{dx^2} + \frac{d^2}{dy^2}\right) + \frac{e^2 B^2}{2m^*}\left(x^2 + y^2\right) + e\,\vec{F}(x,y)\right.$$
$$\left. \bullet \vec{r}(x,y) + V(x,y)\right)\psi(x,y) = E\,\psi(x,y) \tag{2}$$

Where, $m^* (= 0.067m_0)$ [37,38] describes the effective mass of the electron and m_0 is the free electron mass, e is the electron charge, $\vec{P}$ is momentum operator, and $V(\vec{r})$ is the three-dimensional potential. The magnetic field's vector-potential $\vec{A}$ is taken as $\vec{A}(\vec{r}) = (-B\,y, B\,x, 0)$ yielding $\vec{B} = (0, 0, B)$ [39]. $\psi(x,y)$ is the two-dimensional wavefunction for E energy eigenvalues. The electric field is described as $\vec{F}(x,y) = F_x\,\vec{x} + F_y\,\vec{y}$ in two-dimension, $\vec{r}(x,y)$ is the displacement vector, the second-order differential is defined as;

$$\frac{d^2}{dx^2} + \frac{d^2}{dy^2} = -2\,\mathrm{diag}\big(\mathrm{ones}\big(1, N_x N_y\big)\big) + \mathrm{diag}\big(C_{xy}, -N_y\big) + \mathrm{diag}\big(C_{xy}, N_y\big) \tag{3}$$

here $C_{xy} = ones(1,(N_x - 1)N_y)$, N_x and N_y are the length of the matrices to define the QWW region and $V(x, y)$ is the confinement potential,

$$V(x,y) = V(y) + \frac{\Omega}{2\,\pi}\int_0^{2\,\pi/\Omega} V(x + \alpha_0\,\sin\Omega\,t)dt \tag{4}$$

where α_0 is the laser-dressing parameter [40,41] and Ω is the laser frequency [42]. To solve Eq. (2), diagonalization is used in two-dimension. After obtaining the energy levels and wave functions, NOR, SHG, and THG coefficients are calculated as follows [42–44]:

$$\chi_0^{(2)} = \frac{4e^3\sigma_v}{\varepsilon_o}M_{21}^2\delta_{21}\frac{E_{21}^2\left(1 + \frac{\Gamma_2}{\Gamma_1}\right) + \hbar^2\left(\omega^2 + \Gamma_2^2\right)\left(\frac{\Gamma_2}{\Gamma_1} - 1\right)}{\left((E_{21} - \hbar\omega)^2 + (\hbar\,\Gamma_2)^2\right)\left((E_{21} + \hbar\omega)^2 + (\hbar\Gamma_2)^2\right)} \tag{5}$$

$$\chi_{2\omega}^{(2)} = \frac{e^3\sigma_v}{\varepsilon_o}\frac{M_{21}M_{32}M_{31}}{(\hbar\omega - E_{21} - i\hbar\Gamma_3)(2\hbar\omega - E_{31} - i\hbar\Gamma_3/2)} \tag{6}$$

$$\chi_{3\omega}^{(3)} = \frac{e^4\sigma_v}{\varepsilon_o}\frac{M_{21}M_{32}M_{43}M_{41}}{(\hbar\omega - E_{21} - i\hbar\Gamma_3)(2\hbar\omega - E_{31} - i\hbar\Gamma_3/2)(3\hbar\omega - E_{41} - i\hbar\Gamma_3/3)} \tag{7}$$

Here ($E_{fi} = E_f - E_i = \hbar\omega_{fi}$), E_f and E_i are the final and initial energy levels, ε_o is the vacuum permittivity, σ_v is carrier density. ($M_{ji} = \langle\psi_j(x,y)|x|\psi_i(x,y)\rangle$) describes the intersubband dipole moment matrix elements (DMMEs) and δ_{21} ($\delta_{21} = M_{22} - M_{11}$) represents intrasubband DMME.

3. Result and discussion

HHG coefficients were calculated for GaAs/Al$_x$Ga$_{1-x}$As HQWWs whose schematic cross-section was given in Fig. 1. Honeycomb's base lengths were a = 10 nm, $\xi = (a\sqrt{3}/2)$ nm, and the height of the honeycomb was 228 meV which corresponds to x = 0.3 Aluminum concentration [4,28,37], $\sigma_v = 5\times10^{23}\mathrm{m}^{-3}$, and $T_k\left(= {}^1/_{\Gamma_k}\right) = (k = 1, 2, 3)$ are $1, 0.2$, and 0.5 ps [45], respectively. ILF values are going to be given in ξ values now.

Variations of the potential profiles of HQWW with varying ILF for constant EF and MF are shown in Fig. 2. We have aimed to trigger and optimize HHGs. To do that we have simulated the potential profile at first without external fields (Fig. 2a). EF in x and y-directions are applied and it is seen that HQWW is tilted with the effect of EF applied through x and y-directions (Fig. 2b). Then, MF is applied to increase confinement of the carrier as given in Fig. 2c. The varying ILF through x-polarized has been applied for different ξ values (Fig. 2d–f). It is observed that the bottom of the HQWW starts shrinking up to ξ which corresponds to the center point of the honeycomb, then further increase in the ILF value causes structural deformation in HQWW. Symmetry of the hexagon is loosed out because of external fields and HQWW turns into two-quantum well wires for bigger ξ values. The change in QWW is consistent with the result of Niculescu et al. for cylindrical QWW [28].

In Fig. 3, square wave functions (SWFs) of the first four bounded states are plotted without (with) external fields. SWFs of the first four bounded states are shown without external fields in Fig. 3a. All states localize at the center of the HQWW. The distribution of the ground state occurs over a wide area. As a result of hexagonal symmetry, the second and third states have degeneracy and only differ in localization direction through the x and y-axis respectively. As expected, the fourth state is homogeneously distributed in the center. The ground state distribution happens in smaller areas with higher SWF intensity for $F_x = 30$ kV/cm and $F_y = 30$ kV/cm in Fig. 3b. The EF causes broken symmetry and degeneracy is lost between the second and third states. In addition to that, the localization position of the second and third states rotates through the x and y-axis respectively. Due to the tilting effect of the EF, the localization density of the fourth state slightly increases toward the tilted edge of the HQWW. The MF has been applied additionally to the
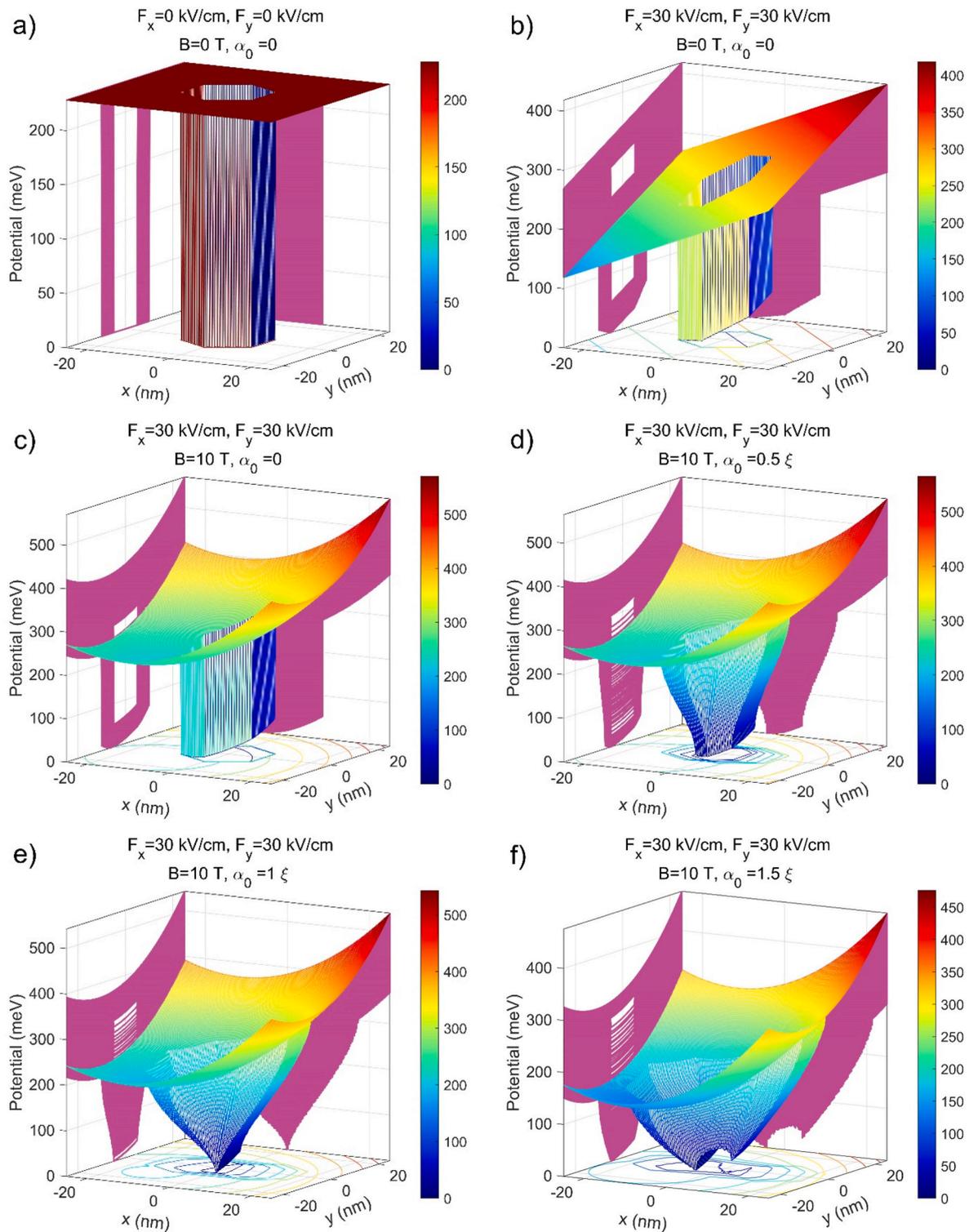
Fig. 2. The potential profiles of GaAs/Al$_x$Ga$_{1-x}$As HQWW for varying ILF under constant EF and MF.

EF as shown in Fig. 3c to increase confinement potential. It is seen that the MF has a minor effect on the localization of all states. In Fig. 3d–f, x-polarization varying ILFs with ξ have been applied to the HQWW for $F_x = 30$ kV/cm, $F_y = 30$ kV/cm and B = 10 T. The ground state localization turns into Gaussian distribution with a higher peak for $α_0 = 0.5$ξ. The ILF shrinks the base of the HQWW and this results in localization of the second state through the x-axis with higher probability. The

same effect is observed for the third state and SWF positions are pushed to be distributed through the y-axis. The localization distribution of the fourth state is less affected than other states. The ground state distribution reaches the highest peak owing to the complete shrinking of the HQWW at the x-axis for $α_0 = $ ξ. The localizations of the second (third) state are pushed in negative and positive directions with lower peaks. The major change is observed for the fourth state, the top of the HQWW becomes wider with higher ILF, and this results in different localization.
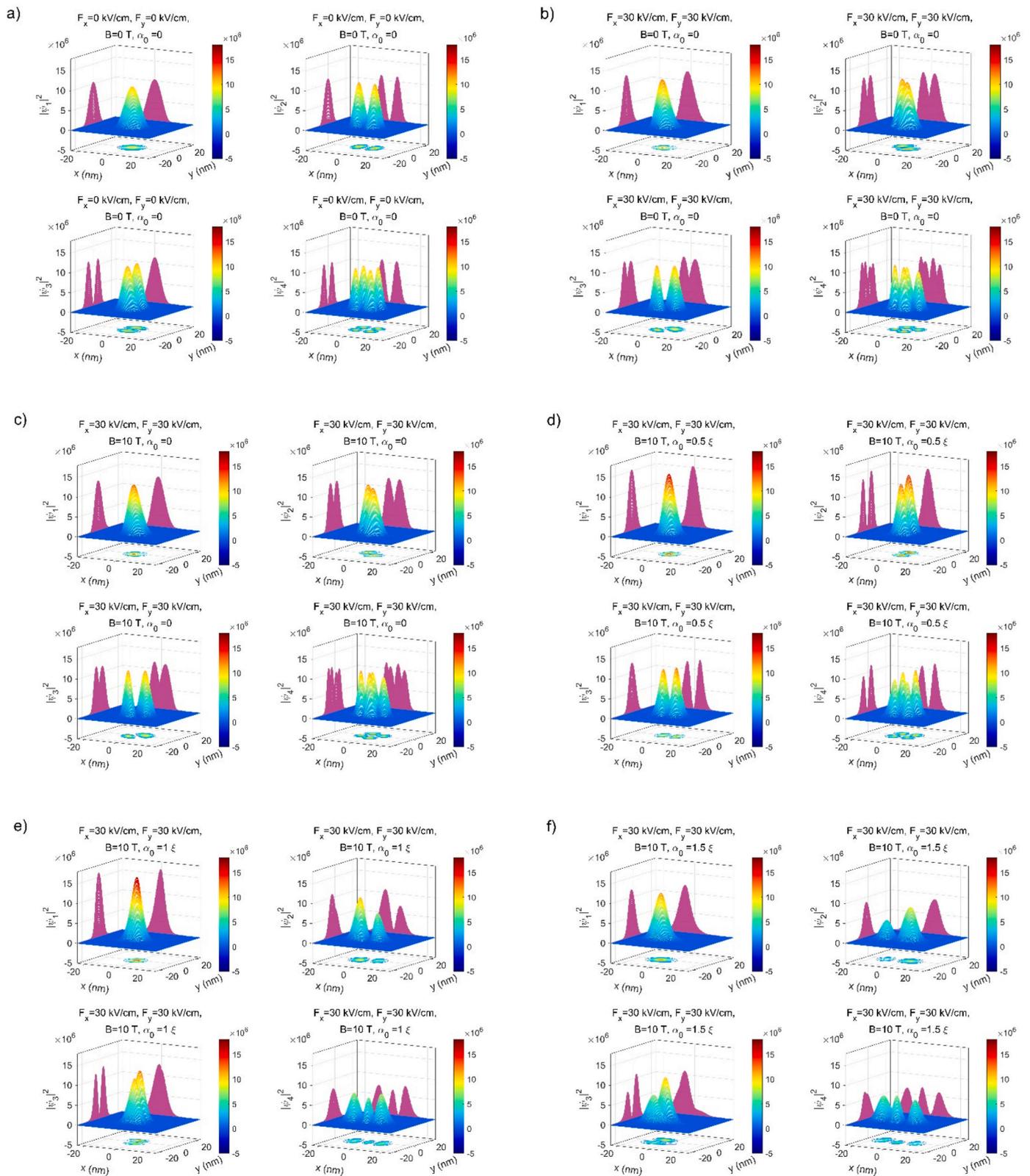
Fig. 3. Square wave functions of the first four bounded energy states of HQWW for varying ILF under constant EF and MF.

Further increase of ILF ($\alpha_0 = 1.5\xi$) causes double QWW in the x-direction and potential height decreases. The localization of all the states happens in a wider area of the QWW region with a lower amplitude of probability as shown in Fig. 3f.

Fig. 4a shows the variation of energy eigenvalues for varying ILF under applied constant EF and MF. All eigenvalues increase up to 0.9ξ, further increase in ILF causes lower energies. It is seen that the second and third states show degeneracy for zero ILF. After ILF of 1.5ξ, the top
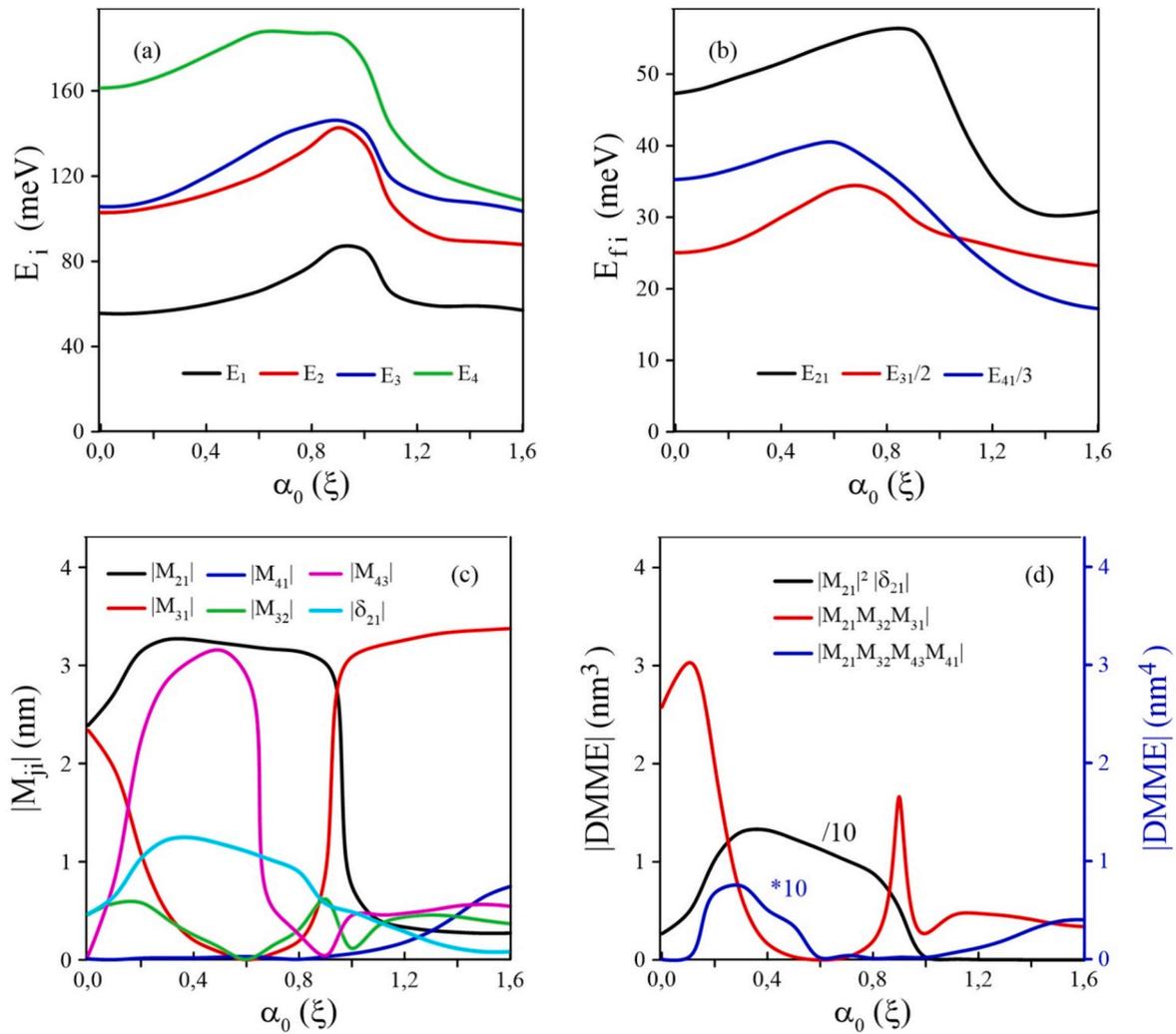
Fig. 4. a) Variation of energy eigenvalues, **b)** transition energies, **c)** $|M_{ji}|$, **d)** product of $|M_{ji}|$ ($|M_{21}|^2|\delta_{21}|$ value is reduced by 10 times and $|M_{21}M_{32}M_{43}M_{41}|$ value is increased by 10 times) for varying ILF for $F_x = 30$ kV/cm, $F_y = 30$ kV/cm and $B = 10$ T.

of the potential profile is widening through the x-direction due to the polarized light. This results in closer energy states and the second, third, and fourth states become degenerate. In Fig. 4b, it is shown that E_{21} increases $0 < \alpha_0 < 0.8\xi$ and decreases $0.8\xi < \alpha_0 < 1.5\xi$ in the ranges then increases for $\alpha_0 > 1.5\xi$. This trend is observed owing to the larger change of the second state than the ground state. $E_{31}/2$ and $E_{41}/3$ are the maximum for 0.7ξ and 0.6ξ and takes the same value at 1.1ξ ILF which is the critical point. Variations of the DMME and their products are given in Fig. 4c and d ($|M_{21}|^2|\delta_{21}|$ value is reduced by 10 times and $|M_{21}M_{32}M_{43}M_{41}|$ value is increased by 10 times). The DMMEs are changed due to the overlap between the wave functions. DMME magnitudes are reaching the maximum and minimum values for different ILF ξ. Properties on the DMMEs are associated with the behavior of the electron wave function and the geometric confinement of electrons in QWs. Multiplication of $|M_{21}|^2|\delta_{21}|$ is maximum at 0.4ξ and suddenly decreases at ξ value and is always smaller for $\alpha_0 > \xi$. $|M_{21}M_{32}M_{31}|$ have two turning points at 0.1ξ and 0.9ξ. The highest magnitude of $|M_{21}M_{32}M_{43}M_{41}|$ products is obtained for 0.3ξ. We can say that DMME products give maxima and minima at different points which is important

for NOR, SHG, and THG coefficients. Energy differences and DMMEs also depend on EF, BF and ILF density for various semiconductor device applications.

The NOR, SHG, and THG coefficients are plotted in Figs. 5–7 under applied external fields. These coefficients are negligible and small for zero external fields (see Figs. 5a, 6a and 7a). To trigger and optimize these coefficients, we have applied EF, MF, and ILF respectively. The MF is applied for having four bounded states otherwise only three energy states are bounded in the HQWW for EF and ILF.

When the EF is applied NOR increases dramatically for $F_x = 30$ kV/cm, $F_y = 30$ kV/cm (Fig. 5b). The MF has a minor effect on the NOR coefficient as shown in Fig. 5c. To maximize the NOR coefficient, ILF is applied. The magnitude of the NOR coefficient depends on the $|M_{21}|^2|\delta_{21}|$ as shown earlier in Fig. 4d. Application of the ILF first increases the magnitude of the NOR coefficient by a factor of five (for 0.5ξ), in agreement with the DMME product, and then causes a drastic decrease as shown in Fig. 5d–f. We think that this is the direct result of the localization position of the wavefunctions due to the deformations in the HQWW shape. The position of the resonance peak of the NOR
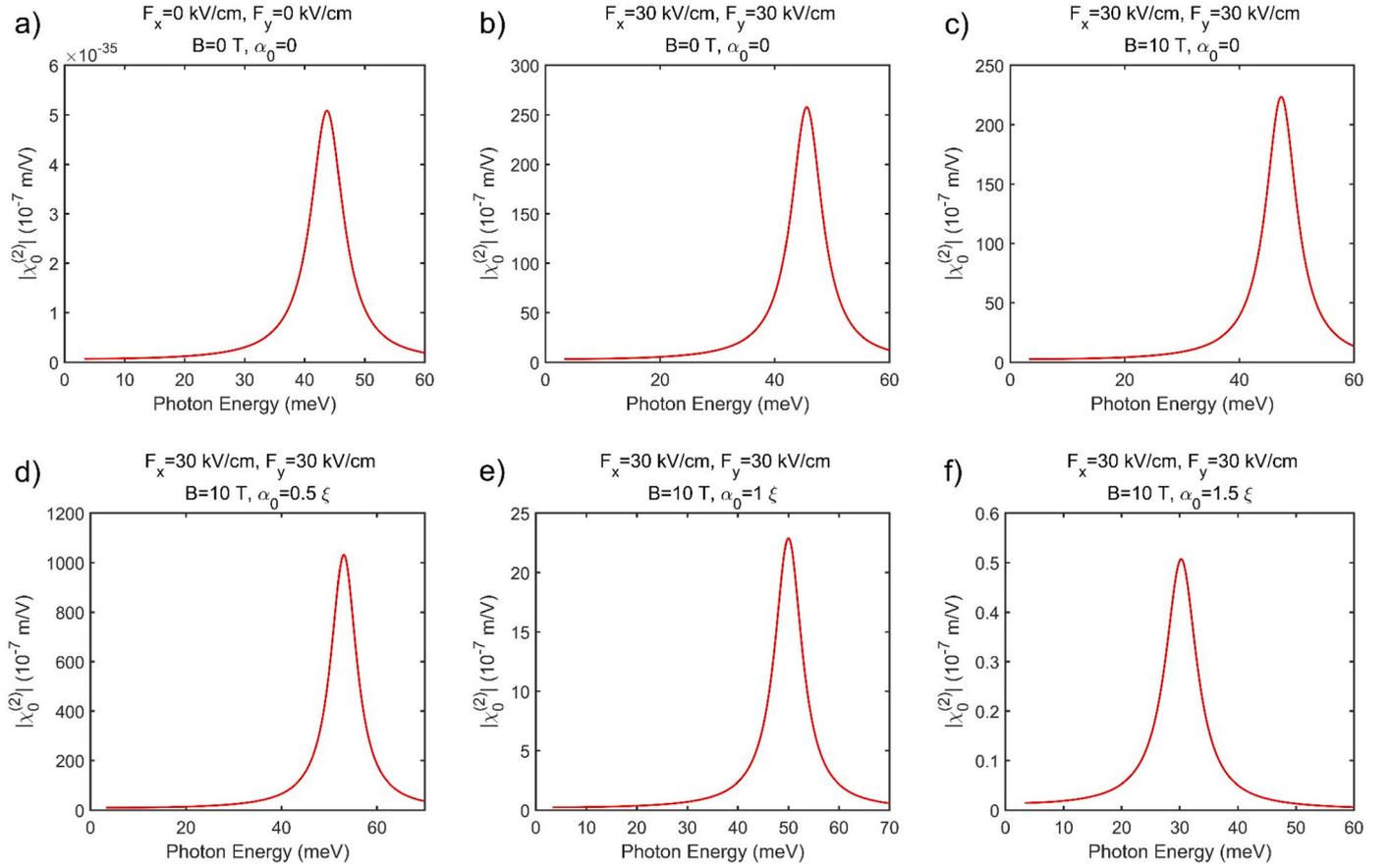
Fig. 5. NOR coefficients with varying ILF for $F_x = 30$ kV/cm, $F_y = 30$ kV/cm and $B = 10$ T.

coefficient is at $E_{21} \approx \hbar\omega$. In addition, blue-shifts are observed for $0 < \alpha_0 < 0.8\xi$ and $\alpha_0 > 1.5\xi$ ranges and redshift is seen for $0.8\xi < \alpha_0 < 1.5\xi$ due to the change of E_{21}.

According to the product of the DMMEs ($|M_{21}M_{32}M_{31}|$), the maximum magnitude of the SHG coefficient occurs for 0.1ξ ($18,4 \times 10^{-7}$ m/V), further increase of ILF causes a sharp decrease in SHG coefficient up to 0.6ξ, then the minor maximum for SHG coefficient happens at 0.9ξ (8.64×10^{-7} m/V). The maximum SHG coefficient is comparable with the experimental result of Boucaud et al., 7.2×10^{-7} m/V, for GaAs/AlGaAs quantum well [46]. This corresponds to almost three times higher SHG coefficient for HQWW than bulk GaAs. Furthermore, Fejer et al. measured the SHG coefficient of the GaAs/AlGaAs superlattice as 0.28×10^{-7} m/V which is matching well with their theoretical results [47]. In comparison with their result, HQWW has a lot higher SHG coefficient. We have attributed this to having such a high SHG coefficient with DMMEs. The resultant position of the resonance peak is at $E_{31}/2 \approx \hbar\omega$ (dominant-major peak) and at $E_{21} \approx \hbar\omega$ (weak-minor peak). The variation of the E_{21} is the same as in NOR coefficients. $E_{31}/2$ shows blue-shift up to 0.7ξ then red-shift is seen for higher ILF values. The maximum distance between major and minor peaks are observed for 0.9ξ (Fig. 6e) and the minimum distance is seen for 1.4ξ (Fig. 6f).

The maxima of the product of the DMMEs occurs for 0.3ξ as $6,2 \times 10^{-15}$ m^2/V^2 but also there are minor maximum which is obtained for 0.7ξ. In addition to maximums, we have observed local minimum while the bottom of the HQWW shrunk ($0.6\,\xi$) and start expanding (0.8ξ) with the effect of ILF. Therefore, the maximum peaks of the THG co-

efficients change depending on the DMMEs' products. The location of the resonance peak is at $E_{41}/3 \approx \hbar\omega$ (dominant-major peak), $E_{31}/2 \approx \hbar\omega$ (middle peak), and at $E_{21} \approx \hbar\omega$ (very weak-minor peak). The change of E_{21} and $E_{31}/2$ are the same as SHG. $E_{41}/3$ shows a blue shift up to an ILF value of 0.7ξ then a red-shift is observed for the rest of the ILF values. The position of the major, middle, and minor peaks in the THG coefficient is the same up to 1.1ξ but after the 1.1ξ ILF value, the position of the major and middle peaks are replaced. This is in line with the energy differences given in Fig. 4b.

4. Conclusion

We have studied the nonlinear optical properties of the HQWW. We have aimed to trigger and optimize HHGs. To do this the constant EF and MF, varying ILF are applied to the HQWW which is made of GaAs/AlGaAs. We have simulated the potential profiles under applied external fields, and it is seen that the bottom of the HQWW is shrinking up to ξ and it turns into a double quantum well wire for ILF over ξ. The position and magnitude of NOR, SHG, and THG coefficients are dependent on the external fields. These are the results of the variation of the DMMEs and the energy difference which are causing red and blue shifts in the optical spectrum. The SHG and THG coefficients are calculated as 18.4×10^{-7} m/V and 6.2×10^{-15} m^2/V^2. SHG coefficient is three times and a lot higher than bulk GaAs and GaAs/AlGaAs superlattice as compared to the values in the literature, respectively. In conclusion, we have shown the effect of the external fields which trigger the HHGs in the HQWW and physical results pointed out the possibility of using HQWW in HHGs semiconductor devices.
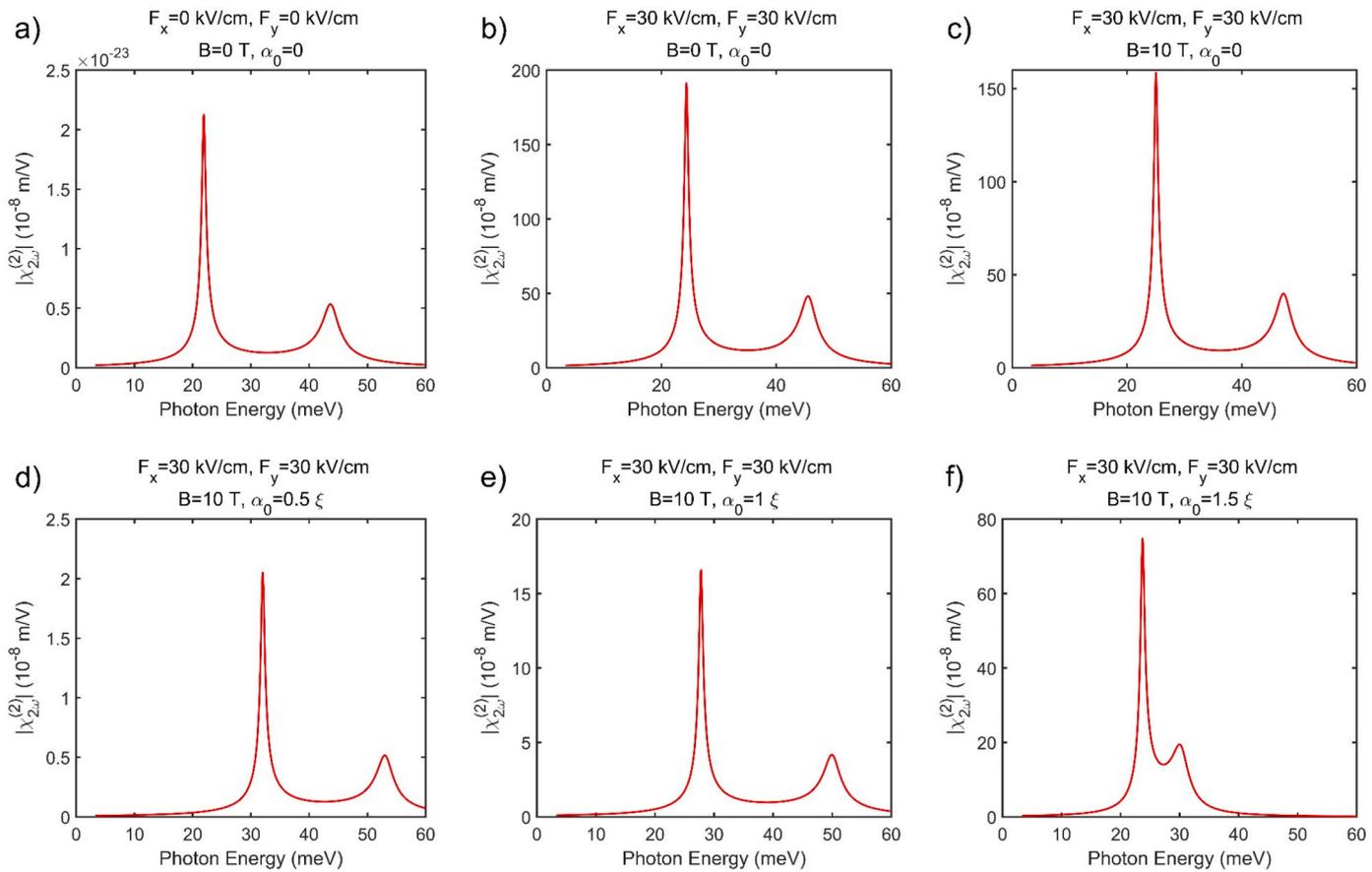
Fig. 6. SHG coefficients with varying ILF for $F_x = 30$ kV/cm, $F_y = 30$ kV/cm and B $= 10$ T.
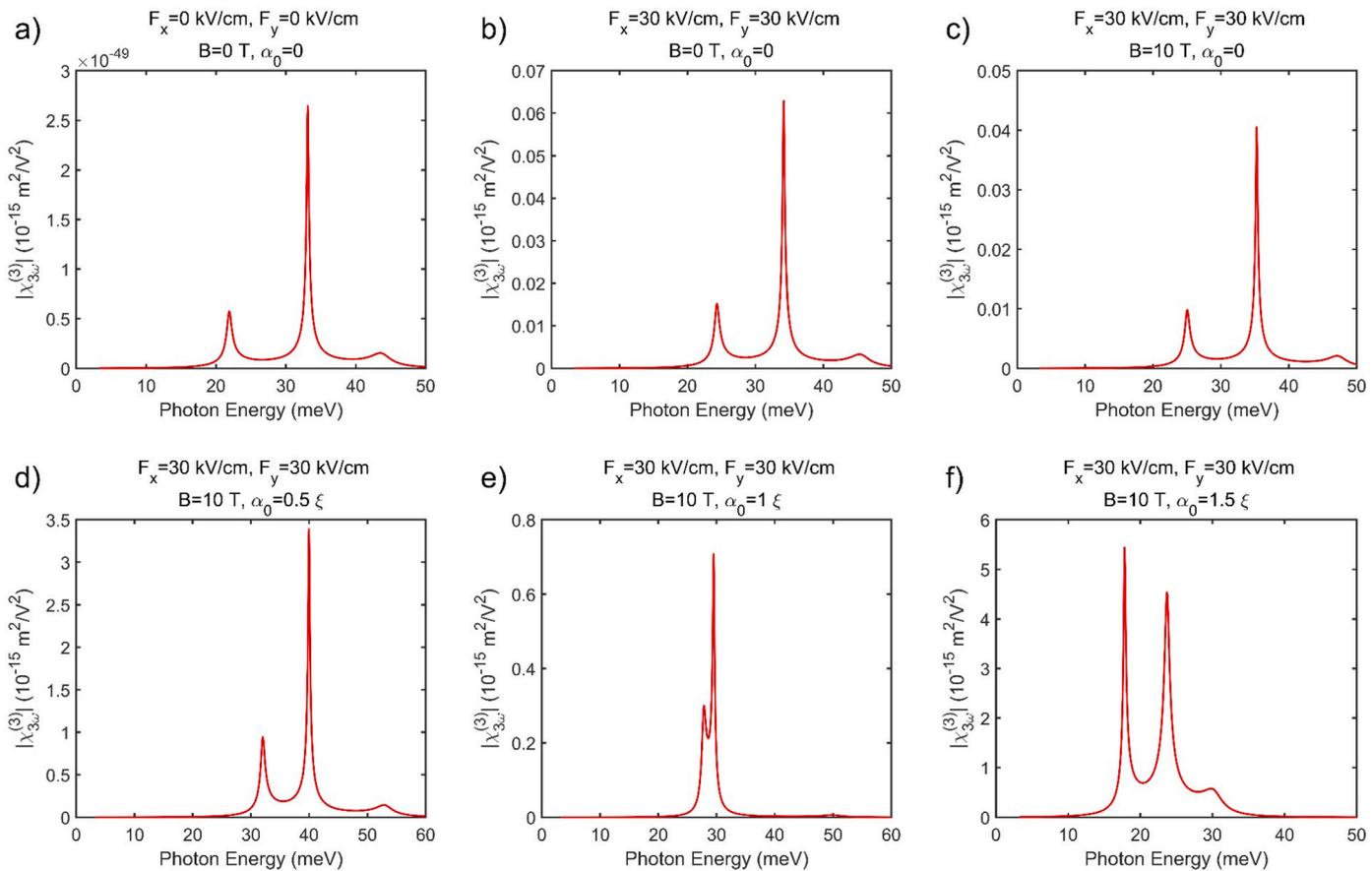
Fig. 7. THG coefficients with varying ILF for $F_x = 30$ kV/cm, $F_y = 30$ kV/cm and B $= 10$ T.

Credit author statement

Asso. Prof. Dr. Behçet Özgür Alaydin contributed throughout whole the manuscript. Assi. Prof. Dr. Didem Altun and PhD candidate Ozan Ozturk contributed to the introduction, data acquisition, graphic drawings, and article writing. Prof. Dr. Emine Ozturk was responsible about whole manuscript parts.

Declaration of competing interest

The authors declare that they have no known competing financial interests or personal relationships that could have appeared to influence the work reported in this paper.

Data availability

The data that has been used is confidential.

References

[1] T. Fei, S. Zhai, J. Zhang, N. Zhuo, J. Liu, L. Wang, S. Liu, Z. Jia, K. Li, Y. Sun, K. Guo, F. Liu, Z. Wang, High power $\lambda \sim 8.5$ μm quantum cascade laser grown by MOCVD operating continuous-wave up to 408 K, J. Semiconduct. 42 (2021): 112301.

[2] B. Heinen, T.-L. Wang, M. Sparenberg, A. Weber, B. Kunert, J. Hader, S.W. Koch, J. V. Moloney, M. Koch, W. Stolz, 106 W continuous-wave output power from vertical-external-cavity surface-emitting laser, in: Electronics Letters, Institution of Engineering and Technology, 2012, pp. 516–517.

[3] L.J. Mawst, D. Botez, High-Power mid-infrared ($\lambda\sim3$-6 μm) quantum cascade lasers, IEEE Photon. J. 14 (2022) 1–25.

[4] D. Altun, O. Ozturk, B.O. Alaydin, E. Ozturk, Linear and nonlinear optical properties of a superlattice with periodically increased well width under electric and magnetic fields, Micro and Nanostructures 166 (2022): 207225.

[5] J. Deng, Y. Zheng, J. Zhou, Z. Li, S. Guo, X. Dai, J. Yu, Z. Ji, Z. Chu, X. Chen, W. Lu, Absorption enhancement in all-semiconductor plasmonic cavity integrated THz quantum well infrared photodetectors, Opt Express 28 (2020) 16427–16438.

[6] H. Yang, Y. Zheng, Z. Tang, N. Li, X. Zhou, P. Chen, J. Wang, MBE growth of high performance very long wavelength InGaAs/GaAs quantum well infrared photodetectors, J. Phys. Appl. Phys. 53 (2020): 135110.

[7] J. Heidrich, M. Gaulke, M. Golling, B.O. Alaydin, A. Barh, U. Keller, 324-fs pulses from a SESAM modelocked backside-cooled 2-μm VECSEL, IEEE Photon. Technol. Lett. 34 (2022) 337–340.

[8] S. Bietti, F.B. Basset, A. Tuktamyshev, E. Bonera, A. Fedorov, S. Sanguinetti, High–temperature droplet epitaxy of symmetric GaAs/AlGaAs quantum dots, Sci. Rep. 10 (2020) 6532.

[9] R.S.R. Gajjela, P.M. Koenraad, Atomic-scale characterization of droplet epitaxy quantum dots, Nanomaterials 11 (2021) 85–108.

[10] E. Koivusalo, J. Hilska, H.V.A. Galeti, Y. Galvão Gobato, M. Guina, T. Hakkarainen, The role of as species in self-catalyzed growth of GaAs and GaAsSb nanowires, Nanotechnology 31 (2020): 465601.

[11] A.G. Saraswathy Vilasam, P.K. Prasanna, X. Yuan, Z. Azimi, F. Kremer, C. Jagadish, S. Chakraborty, H.H. Tan, Epitaxial growth of GaAs nanowires on synthetic mica by metal–organic chemical vapor deposition, ACS Appl. Mater. Interfaces 14 (2022) 3395–3403.

[12] L.-N. Zeng, L. Li, Y.-f. Yang, Z.-y. Liu, Z.-J. Li, Z.-b. Zhao, H. Chen, Z.-L. Qiao, Y. Qu, G.-J. Liu, Morphology characterization and growth of GaAs nanowires on Selective-area substrates, Chem. Phys. Lett. 779 (2021): 138887.

[13] A. Borzdov, V. Borzdov, V. Labunov, V. V'yurkov, Efficiency of Terahertz Harmonic Generation in GaAs Quantum Wire Structure: a Monte Carlo Simulation, SPIE, 2019.

[14] J.A. Gil-Corrales, J.A. Vinasco, A. Radu, R.L. Restrepo, A.L. Morales, M.E. Mora-Ramos, C.A. Duque, Self-consistent schrödinger-Poisson study of electronic properties of GaAs quantum well wires with various cross-sectional shapes, in: Nanomaterials, 2021.

[15] J. Jung, O. Keller, Electrodynamics of a mesoscopic Möbius quantum wire, J. Opt. Soc. Am. B 37 (2020) 3005–3015.

[16] V. Kumar, S.B. Bhardwaj, R.M. Singh, F. Chand, Optical properties and effect of magnetic field on energy spectra of a GaAs spherical quantum dot, European Phys. J. Plus 138 (2023) 191.

[17] X. Li, C. Chang, Nonlinear optical properties of GaAs/AlηGa1$-\eta$As quantum dots system with Hulthén-Yukawa potential, Opt. Mater. 131 (2022): 112605.

[18] E. Rosencher, P. Bois, J. Nagle, E. Costard, S. Delaitre, Observation of nonlinear optical rectification at 10.6 μm in compositionally asymmetrical AlGaAs multiquantum wells, Appl. Phys. Lett. 55 (1989) 1597–1599.

[19] X.H. Qu, H.E. Ruda, S. Janz, A.J. Springthorpe, Enhancement of second harmonic generation at 1.06 μm using a quasi-phase-matched AlGaAs/GaAs asymmetric quantum well structure, Appl. Phys. Lett. 65 (1994) 3176–3178.

[20] M.G. Barseghyan, A.K. Manaselyan, A.A. Kirakosyan, Intersubband absorption in quantum wire with a convex bottom in a magnetic field, J. Phys. Condens. Matter 18 (2006) S2161.

[21] V.N. Mughnetsyan, M.G. Barseghyan, A.A. Kirakosyan, Binding energy and photoionization cross section of hydrogen-like donor impurity in quantum well-wire in electric and magnetic fields, Superlattice. Microst. 44 (2008) 86–95.

[22] G. Liu, K. Guo, Z. Zhang, H. Hassanbadi, L. Lu, Nonlinear optical rectification in laterally-coupled quantum well wires with applied electric field, Superlattice. Microst. 103 (2017) 230–244.

[23] C.M. Duque, M.E. Mora-Ramos, C.A. Duque, Properties of the second and third harmonics generation in a quantum disc with inverse square potential. A modeling for nonlinear optical responses of a quantum ring, J. Lumin. 138 (2013) 53–60.

[24] M.G. Barseghyan, A.A. Kirakosyan, C.A. Duque, Hydrostatic pressure, electric and magnetic field effects on shallow donor impurity states and photoionization cross section in cylindrical GaAs–Ga1–x Alx as quantum dots, Phys. Status Solidi 246 (2009) 626–629.

[25] A. Montes, C.A. Duque, N. Porras-Montenegro, Density of shallow-donor impurity states in rectangular cross section GaAs quantum-well wires under applied electric field, J. Phys. Condens. Matter 10 (1998) 5351.

[26] A. Montes, C.A. Duque, N. Porras-Montenegro, Electric field effects on the states of a donor impurity in rectangular cross-section vacuum/GaAs/vacuum quantum-well wires, J. Appl. Phys. 84 (1998) 1421–1425.

[27] G. Liu, Y. Cao, R. Liu, G. Chen, F. Wu, Y. Zheng, Z. Chen, K. Guo, L. Lu, Terahertz laser field manipulation on the electronic and nonlinear optical properties of laterally-coupled quantum well wires, Opt Express 30 (2022) 5200–5212.

[28] E.C. Niculescu, L.M. Burileanu, A. Radu, A. Lupaşcu, Anisotropic optical absorption in quantum well wires induced by high-frequency laser fields, J. Lumin. 131 (2011) 1113–1120.

[29] M.J. Karimi, G. Rezaei, Magnetic field effects on the linear and nonlinear optical properties of coaxial cylindrical quantum well wires, J. Appl. Phys. 111 (2012).

[30] L.M. Burileanu, A. Radu, THz laser field effect on the optical properties of cylindrical quantum well wires, Opt Commun. 284 (2011) 2050–2055.

[31] A. Montes, C.A. Duque, N. Porras-Montenegro, The binding energies of shallow donor impurities in GaAs quantum-well wires under applied electric fields, J. Appl. Phys. 81 (1997) 7890–7894.

[32] C.A. Duque, A. Montes, A.L. Morales, Binding energy and polarizability in GaAs–(Ga,Al)As quantum-well wires, Phys. B Condens. Matter 302–303 (2001) 84–87.

[33] E.C. Niculescu, M. Cristea, A. Radu, Magnetic field effect on the third harmonic generation in quantum well wires with triangular cross-section, Phys. E Low-dimens. Syst. Nanostruct. 57 (2014) 138–144.

[34] J.-B. Xia, W.-J. Fan, Electronic structures of superlattices under in-plane magnetic field, Phys. Rev. B 40 (1989) 8508–8515.

[35] B.O. Alaydin, D. Altun, E. Ozturk, Linear and nonlinear optical properties of semi-elliptical InAs quantum dots: effects of wetting layer thickness and electric field, Thin Solid Films 755 (2022): 139322.

[36] R.G. Toscano-Negrette, J.C. León-González, J.A. Vinasco, A.L. Morales, F. Koc, A. E. Kavruk, M. Sahin, M.E. Mora-Ramos, J. Sierra-Ortega, J.C. Martínez-Orozco, R. L. Restrepo, C.A. Duque, Optical properties in a ZnS/CdS/ZnS core/shell/shell spherical quantum dot: electric and magnetic field and donor impurity effects, Nanomaterials 13 (2023) 550.

[37] M.J. Karimi, A. Keshavarz, Second harmonic generation in asymmetric double semi-parabolic quantum wells: effects of electric and magnetic fields, hydrostatic pressure and temperature, Phys. E Low-dimens. Syst. Nanostruct. 44 (2012) 1900–1904.

[38] M. Sayrac, J.C. Martínez-Orozco, M.E. Mora-Ramos, F. Ungan, The nonlinear optical rectification, second and third harmonic generation coefficients of Konwent potential quantum wells, Eur. Phys. J. Plus 137 (2022) 1033.

[39] A. Al-Naghmaish, H. Dakhlaoui, T. Ghrib, B.M. Wong, Effects of magnetic, electric, and intense laser fields on the optical properties of AlGaAs/GaAs quantum wells for terahertz photodetectors, Phys. B Condens. Matter 635 (2022): 413838.

[40] M.J. Karimi, H. Vafaei, Second-order nonlinear optical properties in a strained InGaN/AlGaN quantum well under the intense laser field, Superlattice. Microst. 78 (2015) 1–11.

[41] Y.-B. Yu, S.-N. Zhu, K.-X. Guo, Exciton effects on the nonlinear optical rectification in one-dimensional quantum dots, Phys. Lett. 335 (2005) 175–181.

[42] O. Ozturk, B. Alaydin, D. Altun, E. Ozturk, Intense laser field effect on the nonlinear optical properties of triple quantum wells consisting of parabolic and inverse-parabolic quantum wells, Laser Phys. 32 (2022): 035404.

[43] M. Sayrac, Effects of applied external fields on the nonlinear optical rectification, second, and third-harmonic generation in an asymmetrical semi exponential quantum well, Opt. Quant. Electron. 54 (2021) 52.

[44] M. Sayrac, A. Turkoglu, M.E. Mora-Ramos, F. Ungan, Intensity-dependent nonlinear optical properties in an asymmetric Gaussian potential quantum well-modulated by external fields, Opt. Quant. Electron. 53 (2021) 485.

[45] O. Ozturk, E. Ozturk, S. Elagoz, Nonlinear optical rectification, second and third harmonic generations in square-step and graded-step quantum wells under intense laser field, Chin. Phys. Lett. 36 (2019): 067801.

[46] P. Boucaud, F.H. Julien, D.D. Yang, J.M. Lourtioz, E. Rosencher, P. Bois, J. Nagle, Detailed analysis of second-harmonic generation near 10.6 μm in GaAs/AlGaAs asymmetric quantum wells, Appl. Phys. Lett. 57 (1990) 215–217.

[47] M.M. Fejer, S.J.B. Yoo, R.L. Byer, A. Harwit, J.S. HarrisJr, Observation of extremely large quadratic susceptibility at 9.6–10.8 um in electric-field-biased AlGaAs quantum wells, Phys. Rev. Lett. 62 (1989) 1041–1044.